Fuel partialization and power/heat shifting strategies applied to a 30 kW_{el} high temperature PEM fuel cell based residential micro cogeneration plant

Behzad Najafi*

behzad.najafi@polimi.it

Alireza Haghighat Mamaghani

alireza.haghighat@mail.polimi.it

Fabio Rinaldi

fabio.rinaldi@polimi.it

Andrea Casalegno

andrea.casalegno@polimi.it

Dipartimento di Energia, Politecnico di Milano, Via Lambruschini 4, 20156, Milano, Italy

**Corresponding author*. Tel.: +39 02 2399 3840.

Introduction

From the standpoints of crucial climate change arising from greenhouse-gas (GHG) emissions, unavoidable depletion of fossil fuels and upcoming stricter environmental regulations on pollutants emissions, seeking other means of power production based on more efficient and environment-friendly operation has become more and more globally important [1,2]. Fuel cell based micro combined heat and power (micro-CHP) is a viable technology to efficiently cater electricity and heat need of residential dwellings [3,4]. This technology can mitigate the greenhouse gas emissions by utilizing the generated heat during the electricity production to address the thermal need of the residential sector. Furthermore, micro-CHP technology can be a part of the decentralized generation (DG) concept, where energy demands can be met by installing electricity generators close to the users, which brings about improved energy security, lower energy losses from electricity transmission and distribution networks, and possibly reduced energy cost to the consumers [5–7]. Fuel cell-based power generations systems have better performance and lower emissions compared to combustion-based generation technologies at scales from 5 kW to 2 MW [8] while they offer much simpler maintenance requirements. Moreover, combustion-based systems (e.g. internal combustion engines) are not suitable for micro-CHP applications owing to their high thermal-to-electric energy ratio (TER) [9,10]. Fuel cells are electrochemical devices that directly convert the chemical energy of a fuel to electrical energy, without any mechanical intermediate step, which leads to their higher electrical efficiency compared to the most of the conventional devices for power generation [11]. Amongst different types of fuel cell under development, the proton exchange membrane fuel cell (PEMFC) is one of the most promising technologies due to its high power density, rapid start-up, high reliability, low operating temperature, and reduced emissions [12–16]. In this regard, extensive research activities, both experimental and numerical, have been conducted on the development of mathematical models of fuel cells for the purpose of optimization and performance evaluation in both steady state and dynamic conditions [17–20]. The most common type of PEMFC is low temperature PEM (LT-PEM) fuel cell with electrodes based on precious metals which operates at a low temperature (80 °C) and is fed by almost pure hydrogen [21,22]. Although LT-PEM fuel cells are mostly considered for portable applications, when integrated with fuel processor unit with high purity hydrogen reformate output they can be utilized for small scale stationary power production. In this context, Barelli et al. [23] studied the behaviour of an LT-PEMFC based CHP system at variable electrical and thermal load. In another study, Campanari et al. [24] conducted an experiment on a laboratory scale LT-PEMFC based CHP system fed by natural gas with an electrical capacity of about 20 kW_{el}. The reported results showed that even in non-optimized operating condition the system can achieve total efficiency as high as 76% and primary energy saving index of 6%. Nonetheless, a number of disadvantages can be attributed to the LT-PEM fuel cells: high cost of noble catalysts, water management complexity, cooling issues, and CO poisoning [25–27] which encourages researchers and manufacturers to seek solutions and/or alternative options. One way to overcome the above mentioned limits is to increase the operating temperature of the PEM fuel cell to values higher than 100 °C. High operating temperature reduces the cooling requirement, simplifies the water management and lessens the CO adsorption onto the catalyst sites. On the other hand, by operating at higher temperatures not only the electrochemical reaction rates are enhanced, but also the high temperature waste heat can be recovered for cogeneration applications [28–30]. A high temperature PEM (HT-PEM) fuel cell operates at temperatures between 150 °C and 200 °C in which, instead of Nafion-based membranes, PBI (Polybenzimidazole), due to its high thermal stability, is employed. In this regard, several studies investigated the viability of HT-PEM fuel cell for CHP systems for producing electrical and thermal power for small scale applications [31,32]. Zuliani et al. [25] performed an analysis on a micro generation system based on a 1 kW_{el} HT-PEM fuel cell using Aspen Plus software. The obtained results showed that the system can achieve the same electrical efficiency as the one obtained using the LT-PEM based unit while it has a simpler balance of plant. In another research, Arsalis et al. [33] studied the optimization of a 1 kW_{el} HT-PEMFC based micro-CHP using genetic algorithm with net electrical efficiency as the single objective function. Employing the optimization technique by variation of nine decision variables, the net electrical efficiency of the system could reach 0.41, while thermal and total

system efficiency are 0.496 and 0.91, respectively. Furthermore, a long-term analysis of an HT-PEM based micro-CHP in dynamic mode has been investigated by Mocoteguy et al. [30]. Experimental results obtained from their work revealed that in the first 500 h of operation there is no significant drop in stack performance; however after 658 h of cumulated operation the electrical efficiency decreased from 30.6 to 28.3%. On the other hand, economic aspects of the power generation system should always be a part of the whole analysis to evaluate the applicability of the proposed system [34–36]. Guizzi et al. [37] studied the economic and energetic performance of a cogeneration system based on a PEM fuel cell in which pure hydrogen was supplied as the fuel. The generated heat in the fuel cell and reformer was employed to supply the demand of a building, which leads to net electrical and thermal efficiency of 41.93% and 64.16% respectively at rated conditions.

Power generation systems and similarly fuel cell CHP units usually achieve their optimal performance at a specific design point; however it is crucial to any power generation system to operate well also under other conditions according to the customer's requirements and/or environmental changes. In this context, fuel cell-based micro-CHP technology is advantageous since fuel cell can operate more efficiently at part-load operation as well as response rapidly to the load changes [5,38,39]. There are only a few studies available in the literature which investigate the part-load performance of HT-PEMFC based micro-CHP systems. Most of the operational strategies used in previous works are based on the heat-led and electricity-led concepts where the system operates in accordance to the thermal and electrical load demand, respectively. Arsalis et al. [5] studied a residential energy system based on HT-PEMFC and proposed an improved operational strategy to alleviate the shortcomings of conventional strategies such as heat-led and electricity-led. By employing the improved strategy the average net electrical efficiency reached 32.8% in comparison to 31.9% and 27.1% for electricity-led and heat-led strategy, respectively. In another research, Korsgaard et al. [40] performed an analysis on the dynamic performance and the control system of an HT-PEMFC micro-CHP system while taking into account the heat, power and hot water consumption pattern of 25 single family houses in Denmark.

In their previous work [41], the authors proposed a new configuration for an existing LT-PEM fuel cell based residential micro-cogeneration system in which the LT-PEM fuel cell was substituted with a high temperature one. The same configuration has been considered in the present study and different strategies have been applied in order to alter the electrical and thermal generation of the plant. The main objective of the applied strategies is to facilitate addressing different load profiles, which is of great interest in smart grid applications, and to determine the performance of the system at partial load conditions. As the first strategy, fuel partialization method, the fuel provided to the system is gradually reduced and the corresponding electrical and thermal performance indices have been evaluated. In the second strategy, power to heat shifting method, by imposing various current to the stack, the electrical production is reduced while higher thermal power is generated. In the last strategy, the previous strategies are merged and the power to heat shifting method is applied while the system is operating at partial loads. The key advantage of the last strategy compared to the previous ones is that the plant is able to cover a wider range of thermal and electrical demand.

Plant description

Fig. 1 demonstrates the configuration of the HT-PEM fuel cell based CHP plant. Before entering the SMR reactor, natural gas is introduced to the desulfurizer to reach the acceptable level of sulfur content for reforming catalysts. Then, the desulfurized fuel is mixed with the superheated steam coming from the superheater downstream of the SMR reactor (stream 24) and later enters the SMR reactor as a single flow (stream 5). Through the steam reforming reactions take place in the SMR reactor the mixture of CH_4 and H_2O is converted to the hydrogen rich reformate gas including also CO and CO_2 plus a part of the feed which remained unreacted. On the other hand, after providing the required heat for the endothermic reforming reactions in the SMR, the combustion gases leave the SMR reactor still at high temperatures. As a result, the available energy in the combustion gases is firstly extracted in the superheater to provide the required superheated steam for reforming reactions and later in the economizer. Although HT-PEMFC has higher CO tolerance compared to LT-PEMFC, the amount of CO in the syngas is much higher than the acceptable level of CO content for the anodic side of the stack; therefore the SMR outlet stream is introduced into the water gas shift (WGS) reactor in order to decrease the amount of CO via water gas shift reaction and also further production of H_2. Prior to the WGS reactor, a heat exchanger is placed which not only reduces the temperature of the WGS inlet stream, favourable due to exothermic nature of WGS reaction, but also preheats the water before the superheater. The WGS outlet stream passes through the anodic recuperator, a heat exchanger, and finally a water knock out (WKO) before entering the anode of the HT-PEM stack. In the recuperator and the heat exchanger, the temperature of the processed syngas falls down which makes it possible to separate the liquid water from the stream in the WKO. The reformate gas enters the anodic side of the stack where hydrogen is consumed through the electrochemical reaction producing electricity, water and heat. In order to take the most advantage of the unreacted methane and hydrogen in the anodic outlet stream, this stream is directed to the burner. In case the desirable temperature at the burner outlet cannot be reached merely by the combustion of anodic outlet, a separate fuel line and also an air flow have been considered to be injected into the burner. The required oxygen for the cathodic side of the stack is provided by the air compressor upstream of the fuel cell stack. It is noteworthy to mention that cooling of the stack is conducted by an oil circulation which later releases the heat to the Thermal user 1.

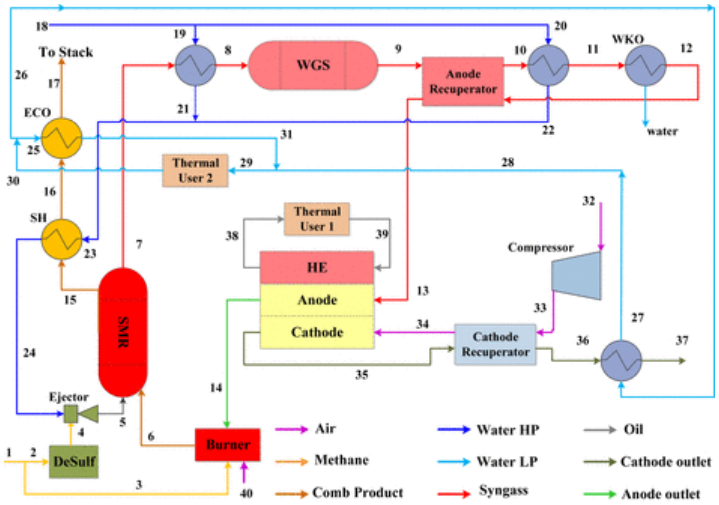

Fig. 1 Schematic view of the HT-PEMFC based CHP plant.

Mathematical model

HT-PEMFC stack

The PEM fuel cell system is described analytically in this section. The fuel cell system mainly consists of the membrane electrode assembly (MEA) where the conversion of hydrogen and oxygen into water takes place, preheater, and the oil cooling system which maintains the temperature of the stack at a desirable level. The reactions occurring in a PEM fuel cell stack are as follows:

$$Anode: H_2 \rightarrow 2H^+ + 2e^- \quad (1)$$

$$Cathode: 2H^+ + \frac{1}{2}O_2 + 2e^- \rightarrow H_2O \quad (2)$$

$$Overall: H_2 + \frac{1}{2}O_2 \rightarrow H_2O \quad (3)$$

As it can be observed from the Equations (1) and (2), hydrogen passes through the anode channels while the air is in the cathodic side. Table 1 summarizes the main geometric parameters of the fuel cell stack used in the modelling process. The MEA can be divided into several parts: cathode and anode channels, the gas diffusion layer (GDL), and the anodic and cathodic electrodes which are separated by the polybenzimidazole membrane. The main task of the electrolyte membrane is to provide a medium for transportation of protons from anode to cathode. Based on the experimental observations, in order to reduce the pressure gradient across the MEA, anode and cathode inlets are supposed to flow in co-current configuration. The MEA domain is simulated with the quasi 2D approach: The domain is divided into infinitesimal elements. One coordinate of integration is considered along the channel, while the other integration coordinate is along the thickness of the MEA. Accordingly since a double integration is performed the model is called 1D + 1D.

Table 1 The geometric parameters of the HT-PEM fuel cell based stack.

Geometric parameter	Value
Channel length (cm)	76.25
Channel height (cm)	0.2
Cell width (cm)	7.6
Number of channels	38
Number of cells	440

The total cell voltage can be formulated as:

$$V = E_{ID} - \eta_{OHM} - \eta_C - \eta_A \quad (4)$$

$$P_{stack} = V_{cell} I_{stack} N \quad (5)$$

where V is the single cell voltage, E_{ID} is the ideal voltage by Nernst equation, η_{OHM} is the ohmic loss, and η_C and η_A are the cathode and anode activation losses respectively.

The Ohmic losses of the electrolyte are calculated using the proton conductivity of the electrolyte:

$$\eta_{ohm} = \frac{i\,\delta_m}{\sigma_{PBI/H_3PO_4}(T)} \quad (6)$$

where

$$\sigma_{PBI/H_3PO_4}(T) = \frac{\sigma}{T} exp\left(-\frac{E_a}{RT}\right) \quad (7)$$

The electrolyte is considered impermeable to the crossing of the reactants gases. Hence, the crossover is considered which can lead to a loss of fuel is considered negligible. The electrolyte conductivity follows Arrhenius law and it is taken from Ref. [42]. In order to simulate the mass transport in the GDL the multi component gas diffusion based on the Stefan–Maxwell phenomenological law has been employed [43].

The losses of cathodic activation represent the most substantial part of the losses in most of conditions. Activation losses are supposed to follow the Tafel Law, first order with respect to oxygen concentration [44]:

$$\eta_C \equiv b \cdot \log\left(\frac{i}{i_*}\right) + b \cdot \log\left(\frac{C_{ref}}{C_{O2,el}}\right) \quad (8)$$

where i_* is the reference exchange current density which follows an Arrhenius like behavior,

$$i^* = i_0^{*,c} \exp\left[-\frac{E_{att}}{R}\left(\frac{1}{T} - \frac{1}{T_{ref}}\right)\right] \quad (9)$$

and b is the Tafel coefficient expressed as $RT/\alpha_C F$ with α_C as the apparent transfer coefficient.

The losses of anodic activation are more complex, since the presence of impurities in the fuel must be taken into account. For instance, the carbon monoxide molecules have a great affinity with the anode catalyst and tend to occupy the active sites which reduces the presence of free sites for the electrochemical reaction. The hydrogen and CO oxidation currents are computed by means of the Butler–Volmer equation [45]:

$$i_{H2} \equiv i_{*,H2} \cdot \vartheta_H \cdot 2 \sinh\left(\frac{\eta_A}{b_A}\right) \quad (10)$$

$$i_{CO} \equiv i_{*,CO} \cdot \vartheta_{CO} \cdot 2 \sinh\left(\frac{\eta_A}{b_A}\right) \quad (11)$$

$$i = i_{CO} + i_{H2} \quad (12)$$

where the coverage of all the species must sum to 1 by definition:

$$\vartheta_{FREE} = 1 - \vartheta_H - \vartheta_{CO} - \vartheta_{H_2PO_4^-} \quad (13)$$

The coverage of phosphoric acid ($\vartheta_{H_2PO_4^-}$) is taken from Ref. [46], and in case of hydrogen and CO, the coverage (ϑ_H and ϑ_{CO}) are computed considering the equilibrium of adsorption using Frumkin adsorption for CO and Langmuir adsorption for hydrogen. It is also noteworthy that the carbon monoxide oxidation is a slow process and then exchange current density of CO ($i_{*,CO}$) is much smaller than that of hydrogen ($i_{*,H2}$).

The values of the parameters used for the HT-PEM fuel cell stack modelling in the present study work are summarized in Table 2.

Table 2 The values of the parameters used for the HT-PEM fuel cell modelling.

Symbol	Value	Description
C_{ref}/mol cm^{-3}	$5.88 \cdot 10^{-6}$	Reference O_2 concentration

δ_{GDL}/cm	0.04	GDL thickness, anode/cathode
δ_{MEM}/cm	0.015	Membrane thickness [37]
ε/τ_{GDL}/–	0.084	Porosity/tortuosity GDL, anode/cathode
$\theta_{H_2PO_4^-}$/–	0.05	$H_2PO_4^-$ coverage [37]
E_0/V	$1.256–2.4\cdot10^{-4}\cdot T$	Ideal potential
α_C/–	0.85	Charge transfer coefficient cathode [33]
E_{ORR}/J mol^{-1}	$102.86\cdot10^3$	Activation energy ORR [37]
$i_{0,ORR}$/A cm^{-2}	$3.28\cdot10^{-6}$	Exchange current density ORR [37]
α_A/–	0.5	Charge transfer coefficient anode [37]
E_{HOR}/J mol^{-1}	$2.5\cdot10^3$	Activation energy HOR
$i_{0,HOR}$/A cm^{-2}	$1.25\cdot10^3$	Exchange current density HOR [36]
$E_{COR,C}$/J mol^{-1}	$127\cdot10^3$	Activation energy COR [36]
$i_{0,COR}$/A cm^{-2}	$2.2\cdot10^{13}$	Exchange current density cathode [36]
$E_{ADS,H}$/J mol^{-1}	$10.4\cdot10^3$	Activation energy hydrogen adsorption [36]
$k_{ADS,H}$/cm s^{-1}	5.96	Hydrogen adsorption constant [36]
$E_{ADS,CO}$/J mol^{-1}	$47.3\cdot10^3$	Activation energy CO adsorption [36]
$k_{ADS,CO}$/cm s^{-1}	$1.5\cdot10^5$	CO adsorption constant [37]
$E_{DES,H}$/J mol^{-1}	$98.3\cdot10^3$	Activation energy hydrogen desorption [36]
$k_{DES,H}$/cm s^{-1}	$2.5\cdot10^3$	Hydrogen desorption constant [36]
$E_{DES,CO}$/J mol^{-1}	$147\cdot10^3$	Activation energy CO desorption [36]
$k_{DES,CO}$/cm s^{-1}	$1.03\cdot103$	CO desorption constant [36]
β_{CO}/–	0.1	Frumkin isotherm symmetry factor [36]
r_{CO}/J mol^{-1} K^{-1}	56.5	Frumkin isotherm lateral interaction parameter [36]
σ_{GDL}/S cm^{-1}	9	GDL conductivity [35]
Σ_0/S cm^{-1} K^{-1}	$9.4\cdot10^3$	Membrane conductivity parameter [33]
$E\sigma_{,MEM}$/J mol^{-1}	$18.5\cdot10^3$	Activation energy membrane conductivity [33]
D_m/cm^2 s^{-1}	0.001	Membrane water permeation coefficient

Fuel processor

Steam methane reformer reactor (SMR)

The steam reformer reactor has the crucial task of converting the natural gas into a hydrogen rich syngas which later fed to the anode. As a result, the performance of the reformer directly affects the electrical power output of the system as well as the

electrical and thermal efficiencies of the plant. In this study, a 1D homogenous model is developed to investigate the behaviour of the steam methane reformer under steady state condition. In order to make the reformer simulation simpler, concentration and temperature gradients in the radial direction are ignored. It is also assumed that the mass transfer between process fluid and the surface of the catalyst is not the rate determining step and the reaction is kinetically controlled. The catalyst composition and structure, due to the confidentiality of the manufacturer's data, cannot be stated. In the reformer model, two separate medium have been considered: the tube side filled with catalyst where the reactions take place and the shell side where the combustion gases coming from burner flow and provide the required heat for endothermic reactions. The accuracy of the model has been checked by comparing the values from the model and the one of experiments conducted on an existing stream reformer. The three main reactions occur in a steam reformer are as follows:

$$CH_4 + H_2O \Leftrightarrow CO + 3H_2 \qquad \Delta H_{298K} = +206\,kJ/mol \tag{14}$$

$$CO + H_2O \Leftrightarrow CO_2 + H_2 \qquad \Delta H_{298K} = -41\,kJ/mol \tag{15}$$

$$CH_4 + 2H_2O \Leftrightarrow CO_2 + 4H_2 \qquad \Delta H_{298K} = +165\,kJ/mol \tag{16}$$

The water gas shift reaction is exothermic and fast enough to be considered in equilibrium. Xu and Froment [47] have developed a general and realistic Langmuir–Hinshelwood type kinetic model for the steam reforming of methane considering the water–gas shift reaction to occur in parallel with the steam reforming reactions. The details of the kinetics of the reforming reactions, kinetic coefficients, and the assumptions can be found in literature [47].

Water gas shift reactor

To optimise the yield of hydrogen and to remove the harmful carbon monoxide, subsequent to the reformer, a WGS reactor is placed. The water gas shift reaction is as follows:

$$CO + H_2O \Leftrightarrow CO_2 + H_2 \qquad \Delta H_{298K} = -41\,kJ/mol \tag{17}$$

The kinetics equation according to Keiksi et al. [48] for high temperature WGS with Fe_3O_4–Cr_2O_3 as catalyst have been utilized. Prior to the WGS reactor, the heat exchanger decreases the temperature of the inlet stream to WGS reactor to a desired level since the WGS reaction is exothermic and favoured by low temperature.

The detailed explanation regarding the steam methane reformer and the water gas shift reactor kinetics can be found in the authors' previous work [41].

Results and discussion

Model validation

In order to evaluate the accuracy of the simulated model of the steam methane reformer and the water gas shift reactor, the obtained results from the models were validated with the experimental ones taken from an LT-PEM fuel cell based CHP plant (Sidera30), designed by ICI Caldaie S.p.A, a prototype of which was previously installed in Department of Energy of Politecnico di Milano. As a result, with the same geometric parameters of the reactors and kinetic characteristics of the catalysts as the real plant as well as the operating condition of the system, the syngas composition at the outlet of the reformer and the WGS reactor obtained by the model were compared with the experimental data. Moreover, the temperature of the syngas leaving the fuel processor reactors and the superheater were compared with the corresponding values extracted from the experimental data. In order to validate the developed model for the HT-PEM fuel cell, the polarization curve of the fuel cell obtained from the model and the experimental data reported by Bergmann et al. [46] were compared. The comparison between the obtained experimental and numerical data from the model has been conducted in the previous works of the authors [34,41].

Performance indices

The most important performance indicators of the plant are defined in this section. The net electrical efficiency ($\eta_{net,el}$), gross electrical efficiency ($\eta_{gross,el}$), and thermal efficiency (η_{th}) have been selected to study the performance of the proposed micro-CHP system.

The net electrical efficiency is defined as the ratio between the net electrical power output and the chemical energy input to the system. The net power output of the system is the power generated by the fuel cell stack after subtracting auxiliaries and losses. The gross electrical efficiency is defined as the ratio of power generated in the stack and the chemical energy input to the system.

$$\eta_{net,el} = \frac{\dot{P}_{el,net}}{\dot{m}_{CH_4,in} LHV_{CH_4}} \tag{18}$$

$$\eta_{gross,el} = \frac{\dot{P}_{el,gross}}{\dot{m}_{CH_4,in} LHV_{CH_4}} \tag{19}$$

The thermal efficiency is defined as the generated heat ($\dot{Q}_{user}$) within thermal user 1 and 2 divided by the chemical energy input to the system.

$$\eta_{th} = \frac{\dot{Q}_{user1} + \dot{Q}_{user2}}{\dot{m}_{CH_4,in} LHV_{CH_4}} \quad (20)$$

The values of $\dot{Q}_{user1}$ and $\dot{Q}_{user2}$ have been calculated based on the energy balance over the fuel cell stack and the low pressure water circuit.

In order to have a proper index to determine the performance of the fuel processor, the reforming factor has been defined as follows:

$$RF = \frac{(\dot{m}_{H_2})_{anode-in} LHV_{H_2}}{(\dot{m}_{CH_4})_{tot} LHV_{CH_4}} \quad (21)$$

wWhere $(\dot{m}_{H_2})_{anode-in}$ is the mass flow rate of hydrogen in the anodic inlet while $(\dot{m}_{CH_4})_{tot}$ is the total mass flow rate of methane which is consumed.

Full load operation

The operating parameters which have been chosen in the present analysis are given in Table 3. It is worth mentioning that in the present work, the fuel fed to the system is composed of 98.36% methane and 1.64% nitrogen (based on molar flow). Taking into account the interconnection between the components of the plant, an iterative procedure has been employed in order to obtain the converged results of the performance of the system. The obtained results demonstrate that the system is capable of producing 27.6 kW of net electrical power and 50.0 kW of thermal power with the net electrical and thermal efficiency of 29.3% and 53.1% respectively.

Table 3 The operating parameters of the HT-PEMFC based CHP plant.

Operating condition	Value
Steam to Carbon Ratio (S/C)	4.5
Auxiliary to process flow rate ratio	0.12
Anodic stoichiometric ratio	1.2
Cathodic stoichiometric ratio	2
Current density (A cm^{-2})	0.2
Combustor outlet temperature (°C)	920
Cell temperature (°C)	160

Fuel partialization approach

As the first strategy, the mass flow rate of the supplied fuel is gradually reduced and the performance of the system at different fuel partialization conditions is monitored. Fig. 2 shows the variations in the gross electrical and thermal generation of the plant while the fuel input is gradually decreased down to 50% of its initial value. As can be observed in this diagram, both the heat and power generations are declining: the electrical generation is diminished from 30.1 kW at full load condition down to 17.3 kW and the thermal generation is reduced from 50.0 kW to 22.4 kW.

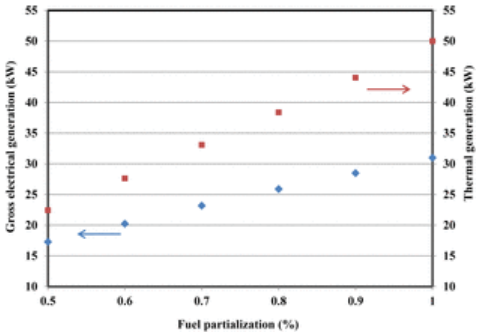

Fig. 2 Variation of gross electrical and thermal generation with fuel partialization.

Given that the provided fuel flow rate is changed in this analysis, while the same fuel processor and stack geometries have been employed, the resulting electrical and thermal performance of the system is expected to be altered. As demonstrated in Fig. 3, fuel partialization leads to an increment in the electrical efficiency and a reduction in the thermal one. The noted gain in the electrical efficiency can be attributed to two different phenomena: the resulting enhancement in the reforming reactions within the steam reformer and the decrement in voltage losses within the stack. However, as demonstrated in Fig. 4, the increment of the reforming factor of the SMR is not noticeable. On the other hand, since less hydrogen is fed to the stack, in order to keep the anodic stoichiometric ratio constant, the current imposed to the stack should be decreased which in turn, as shown in Fig. 5, results in a gradual decrement in the current density. Operation at lower current densities, as can be deduced from the cell's polarization curve, results in lower voltage losses and consequently enhancing the cell voltage from 0.623 V to 0.683 V.

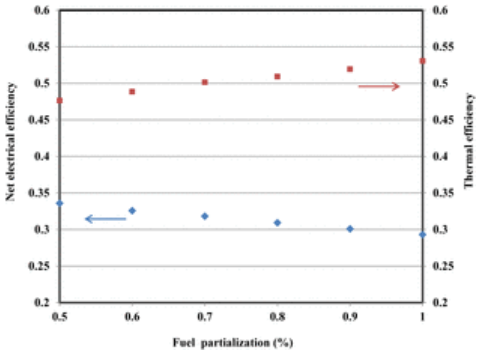

Fig. 3 Effect of fuel partialization on net electrical efficiency and thermal efficiency.

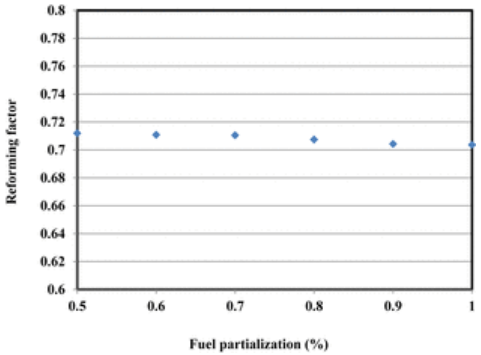

Fig. 4 Variation of reforming factor with fuel partialization.

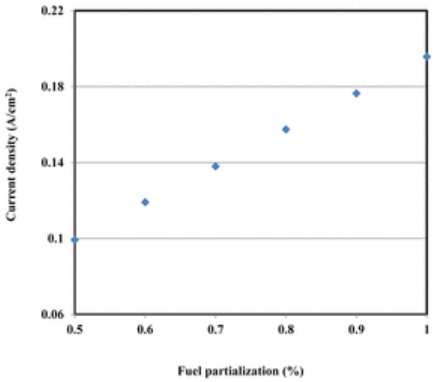

Fig. 5 Variation of current density with fuel partialization.

As can be deduced from the reforming factor trend in Fig. 4, the extent of reforming reactions are slightly increasing; the fact which results in an increase in the molar fraction of carbon monoxide in the anodic inlet stream. Nonetheless, since the resulting CO increase is insignificant, the positive effect of current density reduction is dominant over the negative effect of CO and the obtained voltage is accordingly boosted.

Since the amount of provided fuel to the system is considerably diminishing, the thermal power generated in the stack and economizers and accordingly the overall thermal power output declines. Besides, due to the mentioned decrease in the voltage losses within the stack, the stack's thermal output per specific amount of provided fuel decreases and consequently the overall thermal efficiency of the system will be reduced.

Power/heat generation shifting approach

In order to enhance the generation flexibility of the system while keeping the fuel input unchanged, in the second strategy, the anodic stoichiometric ratio has been employed to switch from the electrical to the thermal generation based on the customer's demand. As it can be seen in Fig. 6, by increasing the anodic stoichiometric ratio, via decreasing the imposed current, the electrical generation of the system decreases from 27.6 to 15.6 kW while the thermal generation is enhanced by 6 kW.

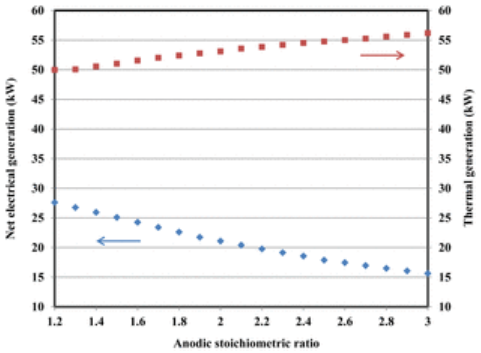

Fig. 6 Variation of net electrical and thermal generation with anodic stoichiometric ratio.

Since the electrical generation is proportional to the product of the cell voltage and the current density, in order to explain the variations in the power output, the effect of changing the anodic stoichiometric ratio on these two parameters should be first investigated in more details.

Increasing the anodic stoichiometric ratio is conducted by decreasing the current imposed to the stack which consequently results in a decrement in the current density. Reducing the current density will lead to an increase in the cell voltage; however, changing the anodic stoichiometric ratio also results in a variation in the profile of CO concentration through the channels of the fuel cell. Fig. 7 shows the profiles of CO dry molar fraction along the channels obtained at different anodic stoichiometric ratios. The observed upward trend of the CO dry molar fraction by increasing the anodic stoichiometric ratio at the inlet of the channels can be attributed to the enhancement in the reforming reactions (especially reaction (1)); while the variation in the anodic stoichiometric ratio has led to a decline in the slope of CO profiles. As can be observed in this figure, by increasing the anodic stoichiometric ratio, the average CO dry molar fraction within the channels is steadily increasing; which consequently can result in a negative effect on the cell voltage. However, due to the dominance of the advantageous effect of the reduction in the current density on the negative effect of the CO molar fraction increment, the overall cell voltage trend is ascending. Accordingly, as it can be observed in Fig. 8, as the anodic stoichiometric ratio is increased, higher values of cell voltage can be achieved.

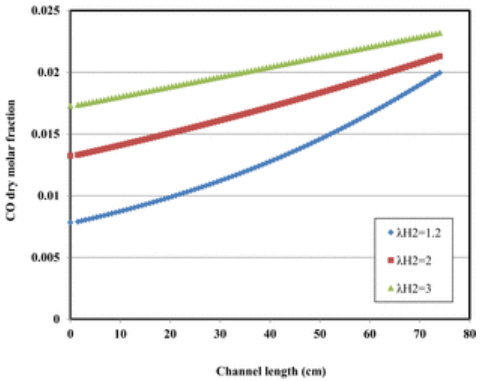

Fig. 7 Effect of variation of anodic stoichiometric ratio on CO dry molar fraction along the channel.

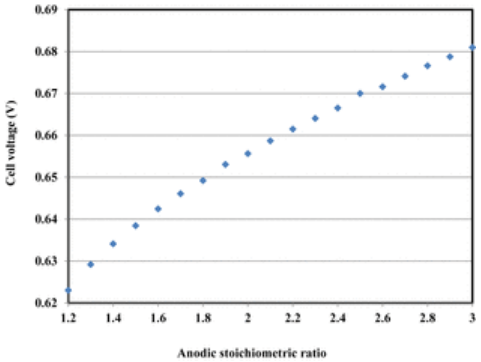

Fig. 8 Variation of cell voltage with anodic stoichiometric ratio.

Nonetheless, due to the fact that the dominant effect of increasing the anodic stoichiometric ratio is the decrement in the current density and not the increment in the cell voltage, eventually the electrical generation deteriorates. As demonstrated in Fig. 9, owing to the witnessed reduction in the generated electrical power, the net electrical efficiency is similarly reduced.

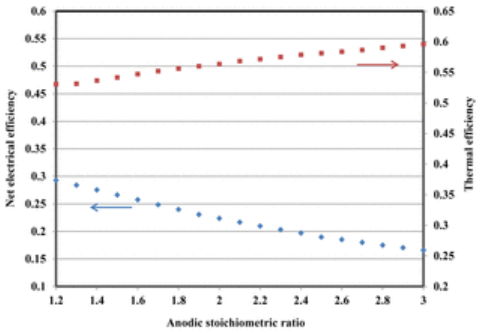

Fig. 9 Effect of anodic stoichiometric ratio on net electrical efficiency and thermal efficiency.

On the other hand, lower amount of available hydrogen for the electrochemical reaction reduces the thermal output of the stack. Imposing higher anodic stoichiometric ratios results in a larger amount of unconsumed hydrogen in the anodic outlet stream which is later injected into the burner, and subsequently augments the heat gain of the economizer. As a result, although the stack's thermal output declines, due to the dominance of the growth in the heat provided in the economizer, the overall trend of the thermal generation is upward. Consequently, the thermal efficiency of the plant, as shown in Fig. 9, experiences an ascending trend. In this context, one can employ the anodic stoichiometric ratio as a useful tool to meet the higher thermal demand during the cold

periods and shift to higher electrical generation during the warm periods.

It is worth mentioning that the two partialization strategies have different impacts on the overall efficiency of the system. In the first partialization method, as stated before, electrical efficiency enhances while the thermal efficiency deteriorates. However, due to the fact that the increment in the electrical efficiency and the decrement in the thermal one have almost the same rate with fuel partialization, a very slight decrease can be observed in the overall efficiency of the system (about 1%). On the contrary, by employing the second approach of partialization, the electrical efficiency experiences a severe plummet (about 13%), while the thermal efficiency only increases by 7%. As a result, the overall efficiency of the system drops from 82.4% at anodic stoichiometric ratio of 1.2 to 76.2% at anodic stoichiometric ratio of 3.

Combined fuel partialization and power/heat shifting approach

Versatility of generation is an important characteristic of a CHP system which can be a crucial factor specifically in smart grid applications. An alternative strategy for covering a wider range of thermal and electrical production is combining the previously discussed fuel partialization and power/heat shifting approaches. In this strategy, by providing less fuel, the thermal and electrical generation of the plant is gradually reduced; while, at each fuel partialization level, the anodic stoichiometric ratio (by changing the imposed current) can be utilized in order to switch between the electrical and thermal generation. Fig. 10 represents the resulting variations in the thermal generation while employing the combined method. As can be observed in this diagram, a wide range of thermal generation starting from 22.4 kW to 56.2 kW can be fulfilled. The resulting heat and power generation map of the system is depicted in Fig. 11 which demonstrates the capability of the system to cater a broad range of electrical demand (8.3 kW to 27.6 kW). Another important advantage of this strategy, as can be noted in the generation map, is that at each specific electrical production, based on the customer's demand, the system can generate different thermal outputs.

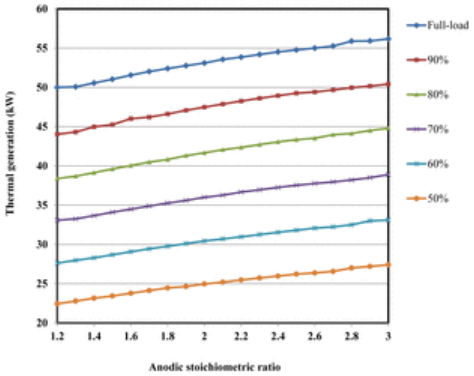

Fig. 10 Thermal generation variation with anodic stoichiometric ratio at different fuel partialization.

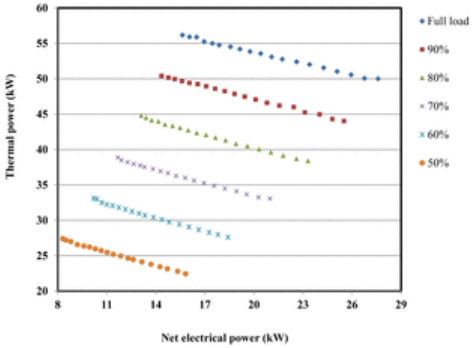

Fig. 11 Electrical-Thermal generation map at different anodic stoichiometric ratio and fuel partialization.

Conclusion

Three different strategies have been proposed and implemented in order to alter the electrical and thermal generation of an HT-PEM fuel cell based CHP plant. In the fuel partialization strategy, the provided fuel was gradually reduced down to 50% of its initial value and it was demonstrated that the gross electrical power is diminished from 30.1 kW at full load condition down to 17.3 kW while the thermal generation is reduced from 50.0 kW to 22.4 kW. In the second strategy,

power/heat shifting, the imposed current of the stack is decreased, resulting in an increment in the anodic stoichiometric ratio, which in turn reduces the net electrical power from 27.6 kW to 15.6 kW while the thermal generation, on the contrary, is boosted by 6 kW. In the last strategy, the first and second approaches are combined; at each fuel partialization level, the anodic stoichiometric ratio is varied. The combined strategy provides a generation map with a wide range of thermal and electrical production and enables the generation of different thermal outputs while producing a specific electrical power.

~~Acknowledgment~~Acknowledgement

This work was carried out in the framework of the project Microgen30 (EE01_00013) funded by Italian Ministry of Economic Development with the program Industria 2015. The authors would also like to acknowledge ICI Caldaie S.p.A for providing technical support for this project.

References

[1]

A. Bazyari, A.A. Khodadadi, A. Haghighat Mamaghani, J. Beheshtian, L.T. Thompson and Y. Mortazavi, Microporous titania–silica nanocomposite catalyst-adsorbent for ultra-deep oxidative desulfurization, *Appl Catal B Environ* **180**, 2016, 65–77.

[2]

A. Haghighat Mamaghani, S. Fatemi and M. Asgari, Investigation of influential parameters in deep oxidative desulfurization of dibenzothiophene with hydrogen peroxide and formic acid, *Int J Chem Eng* , vol 2013, Article ID 951045, 10 pages, 2013.

[3]

T.S. Doyle, Z. Dehouche and S. Stankovic, Decentralized power and heat derived from an eco-innovative integrated gasification fuel cell combined cycle fuelled by waste, *Int J Hydrog Energ* **40**, 2015, 9013–9025.

[4]

C. Robin, M. Gerard, J. d'Arbigny, P. Schott, L. Jabbour and Y. Bultel, Development and experimental validation of a PEM fuel cell 2D-model to study heterogeneities effects along large-area cell surface, *Int J Hydrog Energ* **40**, 2015, 10211–10230.

[5]

A. Arsalis, M.P. Nielsen and S.K. Kær, Application of an improved operational strategy on a PBI fuel cell-based residential system for Danish single-family households, *Appl Therm Eng* **50**, 2013, 704–713.

[6]

A.D. Hawkes and M.A. Leach, On policy instruments for support of micro combined heat and power, *Energy Policy* **36**, 2008, 2973–2982.

[7]

B. Shabani, J. Andrews and S. Watkins, Energy and cost analysis of a solar-hydrogen combined heat and power system for remote power supply using a computer simulation, *Sol Energy* **84**, 2010, 144–155.

[8]

A. Ferguson and V. Ismet Ugursal, Fuel cell modelling for building cogeneration applications, *J Power Sour* **137**, 2004, 30–42.

[9]

A. Arsalis, M.P. Nielsen and S.K. Kær, Modeling and parametric study of a 1 kWe HT-PEMFC-based residential micro-CHP system, *Int J Hydrog Energ* **36**, 2011, 5010–5020.

[10]

A. Haghighat Mamaghani, B. Najafi, A. Shirazi and F. Rinaldi, 4E analysis and multi-objective optimization of an integrated MCFC (molten carbonate fuel cell) and ORC (organic Rankine cycle) system, *Energy* **82**, 2015, 650–663.

[11]

A.J. del Real, A. Arce and C. Bordons, Development and experimental validation of a PEM fuel cell dynamic model, *J Power Sour* **173**, 2007, 310–324.

[12]

J. Marquis and M.O. Coppens, Achieving ultra-high platinum utilization via optimization of PEM fuel cell cathode catalyst layer microstructure, *Chem Eng Sci* **102**, 2013, 151–162.

[13]

R. Othman, A.L. Dicks and Z. Zhu, Non precious metal catalysts for the PEM fuel cell cathode, *Int J Hydrog Energ* **37**, 2012, 357–372.

[14]

K.J. Lange, H. Carlsson, I. Stewart, P.-C. Sui, R. Herring and N. Djilali, PEM fuel cell CL characterization using a standalone FIB and SEM: experiments and simulation, *Electrochim Acta* **85**, 2012, 322–331.

[15]

M. Radulescu, O. Lottin, M. Feidt, C. Lombard, D. Le Noc and S. Le Doze, Experimental and theoretical analysis of the operation of a natural gas cogeneration system using a polymer exchange membrane fuel cell, *Chem Eng Sci* **61**, 2006, 743–752.

[16]

S. Rahimi, M. Meratizaman, S. Monadizadeh and M. Amidpour, Techno-economic analysis of wind turbine–PEM (polymer electrolyte membrane) fuel cell hybrid system in standalone area, *Energy* **67**, 2014, 381–396.

[17]

M. Abdollahzadeh, J.C. Pascoa, A.A. Ranjbar and Q. Esmaili, Analysis of PEM (Polymer Electrolyte Membrane) fuel cell cathode two-dimensional modeling, *Energy* **68**, 2014, 478–494.

[18]

Y. Ding, X. Bi and D.P. Wilkinson, 3D simulations of the impact of two-phase flow on PEM fuel cell performance, *Chem Eng Sci* **100**, 2013, 445–455.

[19]

G. Napoli, M. Ferraro, F. Sergi, G. Brunaccini and V. Antonucci, Data driven models for a PEM fuel cell stack performance prediction, *Int J Hydrog Energ* **38**, 2013, 11628–11638.

[20]

R. Roshandel, F. Arbabi and G.K. Moghaddam, Simulation of an innovative flow-field design based on a bio inspired pattern for PEM fuel cells, *Renew Energ* **41**, 2012, 86–95.

[21]

E. Lechartier, E. Laffly, M.-C. Péra, R. Gouriveau, D. Hissel and N. Zerhouni, Proton exchange membrane fuel cell behavioral model suitable for prognostics, *Int J Hydrog Energ* **40**, 2015, 8384–8397.

[22]

F. Rinaldi and R. Marchesi, Polimeric electrolyte membrane fuel cells: characterization test under variable temperature and relative humidity conditions, *J Fuel Cell Sci Technol* **4**, 2007, 231–237.

[23]

L. Barelli, G. Bidini, F. Gallorini and A. Ottaviano, An energetic–exergetic analysis of a residential CHP system based on PEM fuel cell, *Appl Energ* **88**, 2011, 4334–4342.

[24]

S. Campanari, G. Valenti, E. Macchi, G. Lozza and N. Ravidà, Development of a micro-cogeneration laboratory and testing of a natural gas CHP unit based on PEM fuel cells, *Appl Therm Eng* **71**, 2014, 714–720.

[25]

N. Zuliani and R. Taccani, Microcogeneration system based on HTPEM fuel cell fueled with natural gas: performance analysis, *Appl Energy* **97**, 2012, 802–808.

[26]

A.R. Korsgaard, M.P. Nielsen and S.K. Kær, Part one: a novel model of HTPEM-based micro-combined heat and power fuel cell system, *Int J Hydrog Energ* **33**, 2008, 1909–1920.

[27]

T. Gu, W.K. Lee and J.W.V. Zee, Quantifying the ‘reverse water gas shift’ reaction inside a PEM fuel cell, *Appl Catal B Environ* **56**, 2005, 43–50.

[28]

E. Jannelli, M. Minutillo and A. Perna, Analyzing microcogeneration systems based on LT-PEMFC and HT-PEMFC by energy balances, *Appl Energ* **108**, 2013, 82–91.

[29]

Y. Zhai, H. Zhang, Y. Zhang and D. Xing, A novel H3PO4/Nafion-PBI composite membrane for enhanced durability of high temperature PEM fuel cells, *J Power Sour* **169**, 2007, 259–264.

[30]

P. Moçotéguy, B. Ludwig, J. Scholta, R. Barrera and S. Ginocchio, Long term testing in continuous mode of HT-PEMFC based H3PO 4/PBI celtec-PMEAs for µ-CHP applications, *Fuel Cells* **9**, 2009, 325–348.

[31]

F. Barreras, A. Lozano, V. Roda, J. Barroso and J. Martín, Optimal design and operational tests of a high-temperature PEM fuel cell for a combined heat and power unit, *Int J Hydrog Energ* **39**, 2014, 5388–5398.

[32]

F.J. Pinar, N. Pilinski, M. Rastedt and P. Wagner, Performance of a high-temperature PEM fuel cell operated with oxygen enriched cathode air and hydrogen from synthetic reformate, *Int J Hydrog Energ* **40**, 2015, 5432–5438.

[33]

A. Arsalis, M.P. Nielsen and S.K. Kær, Modeling and optimization of a 1 kWe HT-PEMFC-based micro-CHP residential system, *Int J Hydrog Energ* **37**, 2012, 2470–2481.

[34]

B. Najafi, A. Haghighat Mamaghani, F. Rinaldi and A. Casalegno, Long-term performance analysis of an HT-PEM fuel cell based micro-CHP system: operational strategies, *Appl Energ* **147**, 2015, 582–592.

[35]

A.H. Mamaghani, B. Najafi, A. Shirazi and F. Rinaldi, Exergetic, economic, and environmental evaluations and multi-objective optimization of a combined molten carbonate fuel cell-gas turbine system, *Appl Therm Eng* **77**, 2015, 1–11.

[36]

A. Shirazi, B. Najafi, M. Aminyavari, F. Rinaldi and R.A. Taylor, Thermal-economic-environmental analysis and multi-objective optimization of an ice thermal energy storage system for gas turbine cycle inlet air cooling, *Energy* **69**, 2014, 212–226.

[37]

G.L. Guizzi and M. Manno, Fuel cell-based cogeneration system covering data centers' energy needs, *Energy* **41**, 2012, 56–64.

[38]

P. Costamagna and S. Srinivasan, Quantum jumps in the PEMFC science and technology from the 1960s to the year 2000: part I. fundamental scientific aspects, *J Power Sour* **102**, 2001, 242–252.

[39]

M.L. Perry and T.F. Fuller, A historical perspective of fuel cell technology in the 20th century, *J Electrochem Soc* **149**, 2002, S59–S67.

[40]

A.R. Korsgaard, M.P. Nielsen and S.K. Kær, Part two: control of a novel HTPEM-based micro combined heat and power fuel cell system, *Int J Hydrog Energ* **33**, 2008, 1921–1931.

[41]

B. Najafi, A. Haghighat Mamaghani, A. Baricci, F. Rinaldi and A. Casalegno, Mathematical modelling and parametric study on a 30 kWel high temperature PEM fuel cell based residential micro cogeneration plant, *Int J Hydrog Energ* ***40, 2015, 1569–1583*** ~~2014~~.

[42]

C. Siegel, G. Bandlamudi and A. Heinzel, Systematic characterization of a PBI/H_3PO_4 sol–gel membrane—modeling and simulation, *J Power Sour* **196**, 2011, 2735–2749.

[43]

L. Pisani, Multi-component gas mixture diffusion through porous media: a 1D analytical solution, *Int J Heat Mass Transf* **51**, 2008, 650–660.

[44]

Z. Liu, J.S. Wainright, M.H. Litt and R.F. Savinell, Study of the oxygen reduction reaction (ORR) at Pt interfaced with phosphoric acid doped polybenzimidazole at elevated temperature and low relative humidity, *Electrochim Acta* **51**, 2006, 3914–3923.

[45]

J.J. Baschuk and X. Li, Modelling CO poisoning and O_2 bleeding in a PEM fuel cell anode, *Int J Energ Res* **27**, 2003, 1095–1116.

[46]

A. Bergmann, D. Gerteisen and T. Kurz, Modelling of CO poisoning and its dynamics in HTPEM fuel cells, *Fuel Cells* **10**, 2010, 278–287.

[47]

J. Xu and G.F. Froment, Methane steam reforming, methanation and water-gas shift: I. Intrinsic kinetics, *AIChE J* **35**, 1989, 88–96.

[48]

R.L. Keiski, T. Salmi, P. Niemistö, J. Ainassaari and V.J. Pohjola, Stationary and transient kinetics of the high temperature water-gas shift reaction, *Appl Catal A Gener* **137**, 1996, 349–370.